Coseismic Fault Slip and Transtensional Stress Field in the Hovsgol Basin Revealed by the 2021 Mw 6.7 Turt, Mongolia Earthquake

Xiaoge Liu[1], Wenbin Xu[1,*], Natalia A. Radziminovich[2], Nan Fang[1], Lei Xie[3]

[1]School of Geosciences and Info-Physics, Central South University, Changsha 410083, Hunan, P.R. China

[2]Institute of the Earth's Crust, Siberian Branch of the Russian Academy of Sciences, Lermontov Str., 128, Irkutsk 664033, Russia

[3]The Department of Land Surveying and Geo-Informatics, The Hong Kong Polytechnic University, Hong Kong, China

*Corresponding author: Wenbin Xu (wenbin.xu@csu.edu.cn)

Key points:

- Transtensional coseismic slip and stress field in Hovsgol basin are revealed with InSAR, teleseismic data and focal mechanisms.

- Current deformation of Hovsgol basin is dominated by half-graben forming.

- The 1950 Mondy earthquake may advance the 2021 Turt earthquake increasing potential seismic hazard on the Mondy and South Hovsgol Fault.

Abstract

Knowledge of the regional crustal deformation and stress field is fundamental to understanding and constrain the ongoing Hovsgol basin evolution. The 2021 Mw 6.7 Turt earthquake provides an unprecedented opportunity to probe the local tectonic stress field and upper crust deformation. We investigate the coseismic surface displacements and invert fault slip models using Interferometric Synthetic Aperture Radar observations and teleseismic data. The mainshock occurred as a result of normal faulting with a right-lateral strike-slip component on an NW striking plane, which is consistent with the transtensive local stress field inverted from regional focal mechanisms. Our results also suggest that the current deformation of the Hovsgol basin is dominated by half-graben forming. The 1950 Mondy earthquake may advance the 2021 Turt earthquake by ~7% recurrence interval, meanwhile, the 2021 Turt earthquake may increase the potential seismic hazard on the neighbor Mondy and South Hovsgol Fault, which deserves more attention.

Plain Language Summary

The 2021 Mw 6.7 Turt earthquake has been the strongest earthquake recorded instrumentally for the Hovsgol basin. We used InSAR and teleseismic data to constrain seismogenic fault geometry. InSAR data show the subsidence up to 0.2 m. The comparable normal and strike slip components are found after slip distribution inversions. The maximum coseismic slip was 1.2 m at a depth of 7 km. We also invert the stress fields using the regional focal mechanisms. We found that the 2021 Turt earthquake occurred in the transtensional stress regime, which is consistent with the observed transtensional coseismic slip. Our results also suggest that the current deformation of Hovsgol basin is dominated by half-graben forming. Considering that the earthquake occurred in the junction zone of two large faults, namely the North Hovsgol fault and Mondy fault, an Mw6.9 earthquake occurred on the latter 70 years ago. Based on the Coulomb stress change calculation, we found that the 1950 Mondy earthquake may advance the 2021 Turt earthquake by ~7% recurrence interval, meanwhile potential seismic hazard on the neighbor Mondy and South Hovsgol Fault deserves more attention.

Key words: Coseismic InSAR displacement, Fault geometry and slip distribution, Transtensional stress field, Stress heterogeneity, Half-graben, Coulomb stress change
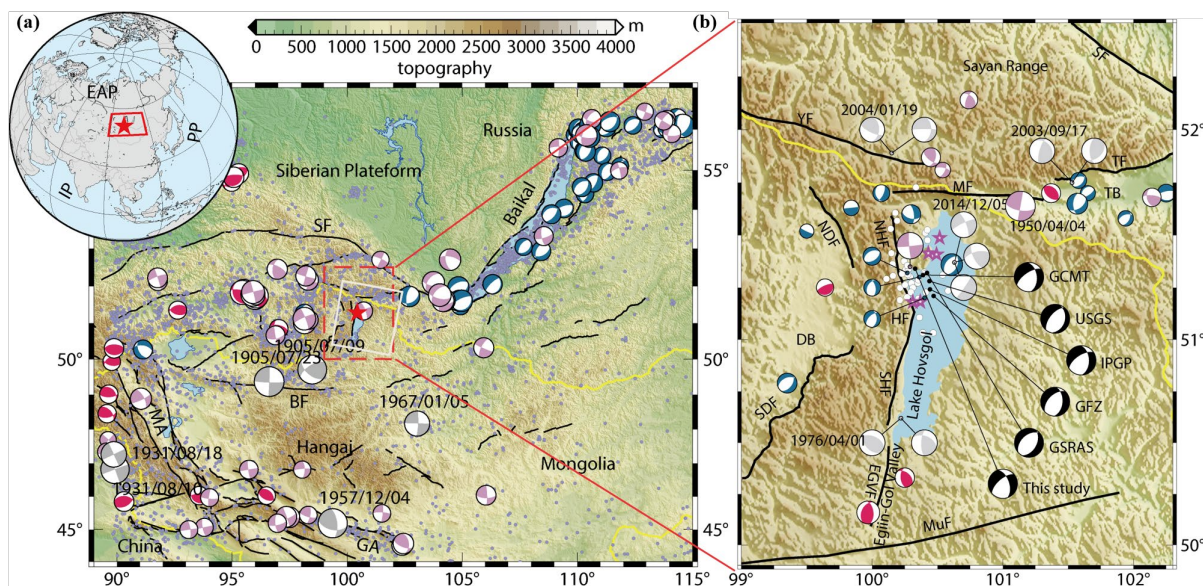
1. Introduction

The Hovsgol basin is situated in the western closure of the Baikal rift system. This rift system is located within the Asian continent interior, and is one of the most active discrete rifts representing the early stages of continental split-up (Petit and Déverchère, 2006). GPS measurements suggest that ~15% of the India-Eurasia convergence (~40 mm/yr) is accommodated within the Baikal Rift System and Mongolia (Calais et al., 2003; Wang and Shen, 2020). The western part of the Baikal rift system is located within the Central Asian mobile belt which traces along the southern margin of the Siberian craton. This belt near the Siberian craton consists of a number of Precambrian and Early Paleozoic terranes (Gladkochub and Donskaya, 2009). The Cenozoic Hovsgol basin has been formed along the border of the Tuva-Mongolian Riphean microcontinent with the early Paleozoic Khamardaban block (Vasiliev et al., 1997). The basin is a half-graben with the steep western side bordered by the Hovsgol master fault. This graben-forming stage is still continuing, which divides the Hovsgol Unit into west-Hovsgol dome-blocky uplift and the east-Hovsgol arch-like structure during the neotectonics stage (Gladkochub and Donskaya, 2009).

The considered area is a key region where compression due to the Indo-Eurasia collision meets extension due to Baikal rifting. In the northern Mongolia, three narrow basins, oriented S-N, namely the Busingol, the Darkhad, and the Hovsgol basins, are supposed to be rift basins; however, the recent stress field here has been evaluated as transpression (Sankov et al., 2011). Reconstructed on tectonic fracturing, slickenside in outcrops of dated Cenozoic formations and basement rocks, the stress field of the Hovsgol basin shows temporal changes from extension in NW-SE direction in Miocene to compression in this direction for a short time in Late Pliocene, and then at the latest stage (Quaternary) to strike-slip and transpression stress field with orientations of NE-SW compression axis and NW-SE tension axis (Sankov et al., 2004). Thus, the present-day stress field in the region is defined as compressional stress regime (Ritz et al., 2000). However, there is no consensus on the type of stress regime in Hovsgol basin. Combined seismological focal mechanisms and geological observations, Delouis et al. (Delouis et al., 2002) provide the stress inversion results indicating the Hovsgol basin is under pure extensive stress regime, while wrench-extensional regime is also proposed for the Hovsgol basin (Petit et al., 1996; Radziminovich et al., 2016). In addition, the seismic

80   focal mechanism solutions of the 2021 Hovsgol mainshock from several organizations

81   showed a consistent normal faulting (Fig. 1b). However, their magnitude of strike slip

82   component and focal depth (10-20 km) is inconsistent (Table 1). These discrepancies indicate

83   that the regional tectonic stress is rather complicated.

84   On 11 January 2021, an Mw 6.7 earthquake occurred in the northern part of the Hovsgol

85   basin. It is the largest instrumentally recorded event here, providing an opportunity for

86   studying the stress heterogeneity in the region. However, only a few geodetic studies were

87   carried out with limited campaign GPS sites (Bayasgalan et al., 2005; Calais et al., 2003;

88   Vergnolle et al., 2003), which are not located in the coseismic region. Fortunately, space

89   geodetic Interferometric Synthetic Aperture Radar (InSAR) technology captures the coseismic

90   surface displacement caused by the 2021 Turt earthquake. This permits us to study the crust

91   deformation and stress regime in the Hovsgol basin. Here, we use Sentinel-1 Synthetic

92   Aperture Radar (SAR) images to map the coseismic InSAR displacements following the 2021

93   Turt Mw 6.7 earthquake. Combining the teleseismic P-wave data, we jointly constrain the

94   seismogenic fault geometry and finite slip model. Using the previous data on earthquake focal

95   mechanisms, we make stress inversion to reveal how the displacement of the Turt earthquake

96   relates to the stress field. Finally, we analyze seismic risk in the Hovsgol region by estimating

97   the Coulomb stress change after the Turt earthquake.

98   **Fig. 1.** Regional seismotectonic context around the 2021 Turt, Mongolia earthquake. (a) Red star represents

99   the epicenter of the main shock from USGS. Blue, pink, and red focal mechanisms represent normal-,

100 strike-slip, and thrust-dominated events from International Seismological Centre (ISC,

101 http://www.isc.ac.uk/iscbulletin/search/fmechanisms/interactive/), respectively. Gray moment tensors are

102 historical great earthquakes with M>7. Purple dots are epicenters for earthquakes since 1900. Black lines

103 are the main active faults from GEM Global Active Faults (https://github.com/GEMScienceTools/gem-

104 global-active-faults). White rectangles represent the spatial extent of Sentinel-1 SAR data from one

105 descending track (DT4). Yellow line shows the border between China, Mongolia and Russia. Dashed red

106 rectangle bounds the extent of enlarged Fig. 1b. The inset shows the location of the study area. IP, Indian

107 Plate; PP, Pacific Plate; EAP, Eurasian Plate. (b) The detailed tectonic background in the study area. Black

108 focal mechanisms represent solutions for the mainshockfrom different catalogs (Table 1). White dots are

109 the aftershocks from USGS, and six Mw > 5 were highlighted by purple starts. SF, Sayan Fault; BF, Bolnay

110 Fault; TF, Tunka Fault; MF, Mondy Fault; YF, Yamaatinskiy Fault; HF, Hovsgol Fault including North HF

111 (NHF) and South HF (SHF); NDF, North Darkhat Fault; SDF, South Darkhat Fault; EGVF, Egiin-Gol

112 Valley Fault; MuF, Murn Fault; MA, Mongolian Altay; GA, Gobi Altay; TB, Tunka Basin; DB, Darkhat

113 Basin. Note that the SHF and MuF are compiled from previous studies and geomorphology (Jolivet et al.,

114 2013; Petit et al., 2002; Ritz et al., 2018; Schlupp and Cisternas, 2007).

2. Data Processing and Inversion Methods

2.1. Coseismic Data Processing

2.1.1. InSAR Data

118 The Turt earthquake occurred in the remote northwestern of Mongolia, where few in-situ

119 geodetic observations (i.e., GPS) are available near the epicenter (Calais et al., 2003; Wang and

120 Shen, 2020). However, the good condition of arid climate and low erosion rates (Meltzer et al.,

121 2019) permit us to employ InSAR technology to obtain the space geodetic displacements for

122 this earthquake even with the C-band SAR images. SAR data acquired by the Sentinel-1

123 satellite provide a unique opportunity to quantify surface displacements of the Turt earthquake

124 and to constrain the activated normal fault structures beneath the Lake Hovsgol (Fig. 1).

125 Using the Gamma software (Wegmuller et al., 2015), high-accuracy coregistration of the

126 primary and secondary Single Look Complex (SLC) products from descending tracks were

127 firstly carried out (Table S2). Then, we constructed coseismic interferograms with the

128 coregistrated primary and secondary SLCs. After removing the effect of topography with the

129 30 m Shuttle Radar Topography Mission digital elevation model (Farr et al., 2007), an improved

130   power spectrum filter method was applied to minimize the phase noise in the interferograms

131   (Li et al., 2008). We unwrapped the filtered pairs of interferograms by a minimum cost flow

132   method (Chen and Zebker, 2001), and geocoded the unwrapped interferograms to obtain the

133   coseismic surface displacement fields. Considering the substantial topographic relief

134   surrounding the Lake Hovsgol, possible topography-dependent tropospheric delay was

135   estimated and removed (Xu et al., 2017).

136

137   **2.1.2. Teleseismic Data**

138   In addition to InSAR data, we also collected P wave records from 43 teleseismic stations

139   at epicentral distances between 30° and 90° (Fig. S1) compiled by the Incorporated Research

140   Institutions for Seismology (IRIS). The initial P wave records were firstly processed to

141   minimize the influence of instrument response (Wald et al., 1996), and then a band-pass filter

142   (0.01-0.5 Hz) was applied to suppress the noises. In addition, the teleseismic stations in the

143   southern azimuth were excluded due to the low signal-to-noise ratio. Time window of

144   waveforms was tapered as 98 s with 30 s before the initial arrivals (Figs. 2 and S2). The

145   global velocity model AK135 is used for teleseismic Green's function calculation.
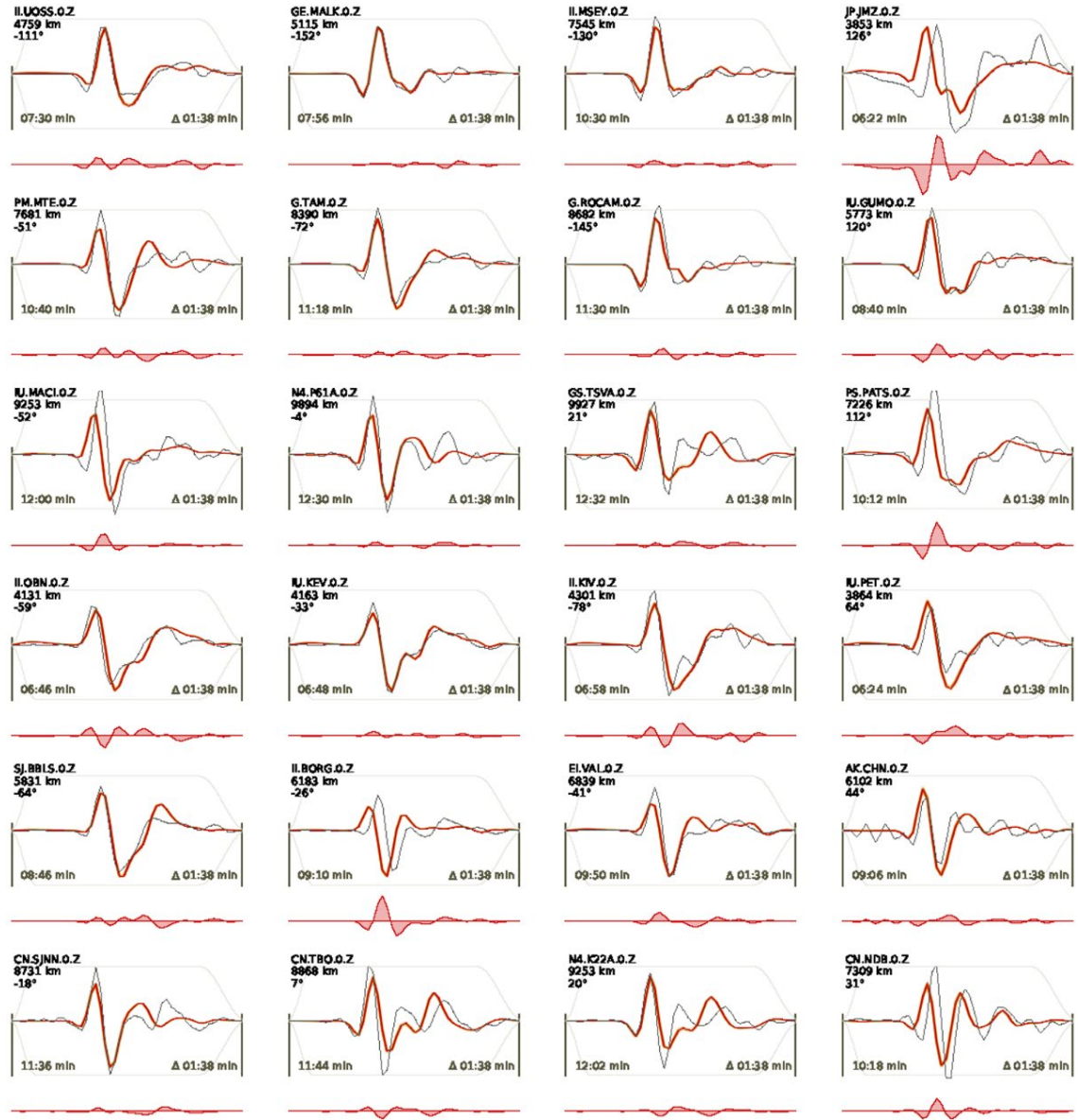
Fig. 2. Comparison between the observed teleseismic P waves and the synthetic waveforms obtained from the joint inversion of uniform fault slip model. The filtered (0.01–0.1 Hz) displacement waveform data (gray line) and the filtered synthetic displacement waveforms (red line) are shown together. Brown shading indicates 100 random draws of the filtered synthetic waveform displacements from the posterior probability density. Red-line polygons below each waveform submap represent the residual waveforms. Each sub-panel is annotated with the station name, component, the distance, and azimuth angle from the maximum a-posterior solution from the center of the reference fault. The arrival time and the duration of each station are shown in the lower left and right, respectively.

2.2. Fault Geometry and Distributed Slip Inversion

158   Before making an inversion of the Turt earthquake seismogenic fault geometry, we first

159   downsampled the InSAR interferograms with a quadtree algorithm (Jónsson et al., 2002) to a

160   computationally tractable size. Covariances of the downsampled data are estimated with the

161   variability of raw observations within the downsampled grids and employed to weight the

162   observations in the following inversions. In order to provide extra constrain on the fault

163   geometry, P wave records data from IRIS and GEOFON are also introduced. The variances of

164   P-wave data are estimated based on the data fluctuation before the P-wave arrival time.

165   Bayesian Earthquake Analysis Tool (BEAT) is applied to determine the fault geometry

166   parameters and their uncertainties (Vasyura-Bathke et al., 2020). To broadly cover the solution

167   space and better quantify the associated uncertainties, a relatively loose sampling boundary is

168   set up for fault geometry parameters according to prior knowledge (e.g., focal mechanisms

169   from USGS/GCMT/GFZ/IPGP/GSRAS etc.) (Table 1 and Table S3). More detailed

170   information about the nonlinear inversion can be found in (Vasyura-Bathke et al., 2020).

171   To resolve a distributed slip coseismic model fitting the observations better, we fixed the

172   fault geometry derived from joint InSAR and teleseismic data inversion and extended the

173   fault size with length of 50 km and width of 30 km (24 km in depth), and the fault was

174   divided into 2×2 km subfaults. Being more finely discretized, sources are generally

175   overparameterized, which commonly requires smoothness constraints to stabilize the

176   solutions (Jónsson et al., 2002; Xu, 2017). We used the Laplacian regularization with smoothing

177   factor determined from Cholesky decomposition of off-diagonal terms in a Gaussian

178   prior $p(\mathbf{s}|\alpha)$. The maximum-a-posterior solution for strike, dip, and slip and the Laplacian

179   smoothing factor α is obtained with sequential Monte Carlo method (Del Moral et al., 2006).

180   More detailed information can be found in (Vasyura-Bathke et al., 2020).

181

2.3. Focal mechanism data and stress inversion

183   To make stress field inversion, we compiled a database of focal mechanism solutions for

184   the Hovsgol region which come mainly from regional solutions published in the regular

185   catalogs and some papers. The dataset includes focal solutions for 27 earthquakes that

186   occurred before the 2021 Turt event (Table S1, Fig. 6). The vast majority of mechanisms were

187   determined by the method of first motion polarity of P waves at the regional stations. Four

188   earthquakes have several solutions obtained by different authors. The strongest earthquake in

189   the area is the 1950 Mw6.9 Mondy earthquake occurred at the western termination of the

190   Tunka basins. Its fault-plane solution discussed in detail in (Delouis et al., 2002) was a sinistral

191   strike-slip movement on the western sublatitudinal segment of the Mondy fault. Other faults

192   in the western Tunka area have a reverse fault component that led to the conclusion about the

193   strike-slip or transpressive stress field here (Delouis et al., 2002; Radziminovich et al., 2016;

194   Sankov et al., 2004). However, the northern part of the Hovsgol basin is characterized mainly

195   by normal faulting in earthquake foci (Fig.1b, 5), though the 2014 Mw4.9 earthquake, which

196   occurred closer to the eastern side of the northern Hovsgol, had a different mechanism. Three

197   solutions are available for it (Table S1): the GCMT solution is a strike-slip with a normal fault

198   component, the first-motion solution is pure dip-slip with a flat and a steep planes of the NE

199   orientation (Dobrynina et al., 2018), and strike-slip solution with a reverse component is based

200   on the surface waves inversion (Melnikova et al., 2020). In contrast to the northern part of the

201   Hovsgol basin, its southern part is distinguished by reverse faulting (Figs. 1 and 5).

202   There are several methods for determining tectonic stress from focal mechanisms. The

203   most commonly used methods have been developed by (Gephart and Forsyth, 1984; Michael,

204   1984; Michael, 1987), which have been expanded and modified by (Lund and Slunga, 1999;

205   Martínez-Garzón et al., 2016; Vavryčuk, 2014). An iterative joint inversion method (Vavryčuk, 2014)

206   was adopted to calculate triaxial stress field σ_1, σ_2, σ_3 with $\sigma_1 > \sigma_2 > \sigma_3$ under the positive

207   compression stress convention, and the stress shape ratio $R = (\sigma_1 - \sigma_2)/(\sigma_1 - \sigma_3), 0 \leq R \leq 1$

208   describing the relative magnitudes of the principal compressive stresses (Warren-Smith et al.,

209   2019). This method is suitable for regions without information about actual tectonic faults.

210   This is attributed to a fault instability algorithm identifying a more likely nodal plane (Lund

211   and Slunga, 1999; Vavryčuk et al., 2013), which has little influence on the accuracy of stress field

212   orientations but significant improvement on the stress shape ratio. Additionally, this method

213   allows one to quantify the confidence intervals of optimal stress tensor by bootstrap

214   resampling approach (Michael, 1987), in which each nodal plane can be selected with equal

215   probability during the sampling.

216   For stress inversion, we used the focal mechanisms of earthquakes which occurred

217   before the Turt earthquake (Table S1, Fig.5) and the main shock (our solution) (Table 1 and

218   Table S1). Two samples were taken: the total sample given in Tables and only for the northern

219   part of the Hovsgol area. We estimated 2000 bootstrap samples with random noise 10° to

220   obtain 95% confidence region of optimal stress tensor. The average misfit angle α between

221   the observed and predicted fault slip directions can be used to evaluate the success of stress

222   inversion.

223

3. Results

3.1. Coseismic InSAR displacement of the 2021 Turt earthquake

226   The excellent coherence and generally low noise level in the coseismic interferogram

227   characterize well-defined surface displacements associated with the Turt earthquake (Fig. 3).

228   The displacements are mainly distributed between the North Hovsgol Fault (NHF, Fig. 3) and

229   west bank of Lake Hovsgol. Few coseismic displacement can be observed on the neighboring

230   NNE-SSW striking South Hovsgol Fault (SHF), which may inhibit propagation of coseismic

231   rupture (Wilson et al., 2009). The descending coseismic displacement field shows obvious up to

232   ~20 cm surface subsidence away from the satellite line of sight (LOS) direction, indicating the

233   significant displacement zone is located at the hanging wall of the normal fault. There is no

234   obvious range decrease in the radar LOS direction except for the about ~5 cm LOS uplift

235   along the east bank of Lake Hovsgol (Fig. 3a). Interestingly, there exists a secondary fault

236   (NDF) on the west side of the seismogenic fault (~25 km), which may constrain the surface

237   displacement patterns on the footwall side of NHF (Fig. 3). It is worthy to note that coseismic

238   interferogram covers six Mw 5 and other aftershocks, which occurred on the same day of the

239   mainshock. In addition, the descending coseismic displacement contains more than one day of

240   other postseismic transients. These indicate that the coseismic displacements may be affected,

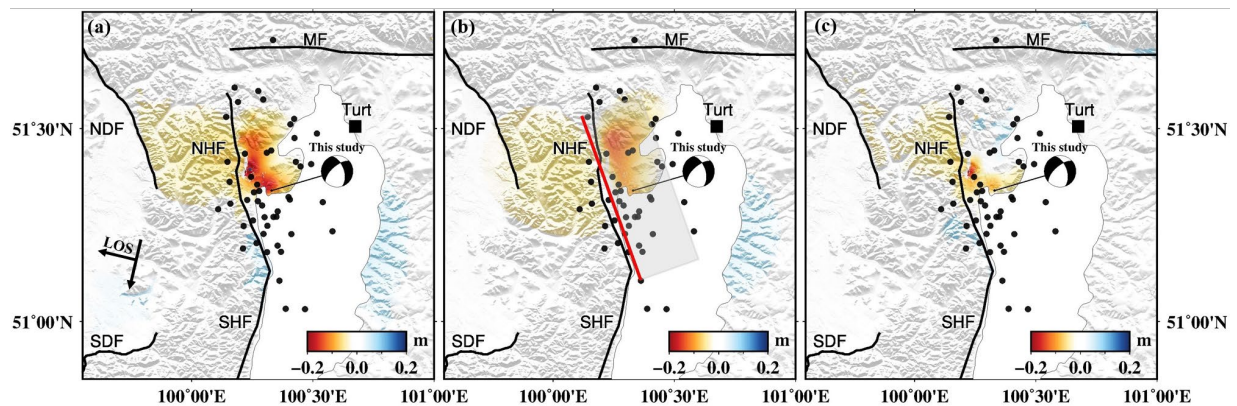241   to some extent, by postseismic activities (Liu and Xu, 2019).

242

244   **Fig. 3.** Observed and modeled coseismic ground displacements in satellite line of sight (LOS)

245   direction. (a) the observed ground deformation fields; (b) model predictions; (c) residuals

246   between observations and models. Black moment tensor and dots represent USGS solution

247   and aftershocks. The shade box in (b) represents the ground projection of the seismogenic

248   fault with the red solid line indicating the fault trace. The fault abbreviations are identical to

249   those in Fig. 1.

250

251   **3.2. Fault Geometry and Slip Distribution**

252   There are several fault-plane solutions for the Turt earthquake issued by different

253   seismological agencies (Table 1). After the complete solution search for strike [0°, 360°], dip

254   [0°, 90°], and rake [-180°, 180°] angles (Table S3), our results of nonlinear inversion show

255   that the optimal fault plane was the NNW-SSE oriented plane (Table 1, Table S3). This

256   confirms that the NHF is the seismogenic fault nucleating the 2021 Turt earthquake. The

257   maximum posterior probability uniform slip model solution obtained after 10^6 iterations with

258   sequential Monte Carlo method, raising the preferred fault plane of 35 km long and 14 km

259   wide with a strike angle of 341°, a dip angle of 54°, and a rake angle of -146° (Table 1). This

260   is consistent with the field-mapped fault trace along the west side of Lake Hovsgol (Fig. 1)

261   and explains well the observed P waveform data (Fig. 2). Trade-offs between the fault

262   parameters are not obvious (i.e., strike, dip and rake angles) as shown in the histograms of

263   posterior probability distributions (Fig. 4).

264

265   **Table 1.** Source parameters for the 2021 Turt earthquake. USGS, U.S. Geological Survey

266   (https://earthquake.usgs.gov);   GCMT,   Global   Centroid-Moment   Tensor   Project

267   (https://www.globalcmt.org/); GFZ, GeoForschungsZentrum (GEOFON) Moment Tensor

268   Solutions (http://geofon.gfz-potsdam.de/eqinfo/); IPGP, Institute de Physique du Globe de

269   Paris (http://www.ipgp.fr/fr); GSRAS, Geophysical Survey of Russian Academy of Sciences

270   (http://www.ceme.gsras.ru/new/ssd_news.htm).

Source	Lon (°)	Lat (°)	Depth (km)	Strike (°)	Dip (°)	Rake (°)	*Mw*
USGS	100.438	51.281	11.5	16/219	32/60	-110/-78	6.74
GCMT	100.39	51.31	14.3	354/236	45/65	-143/-52	6.8
GFZ	100.47	51.21	18	4/226	47/51	-121/-60	6.7

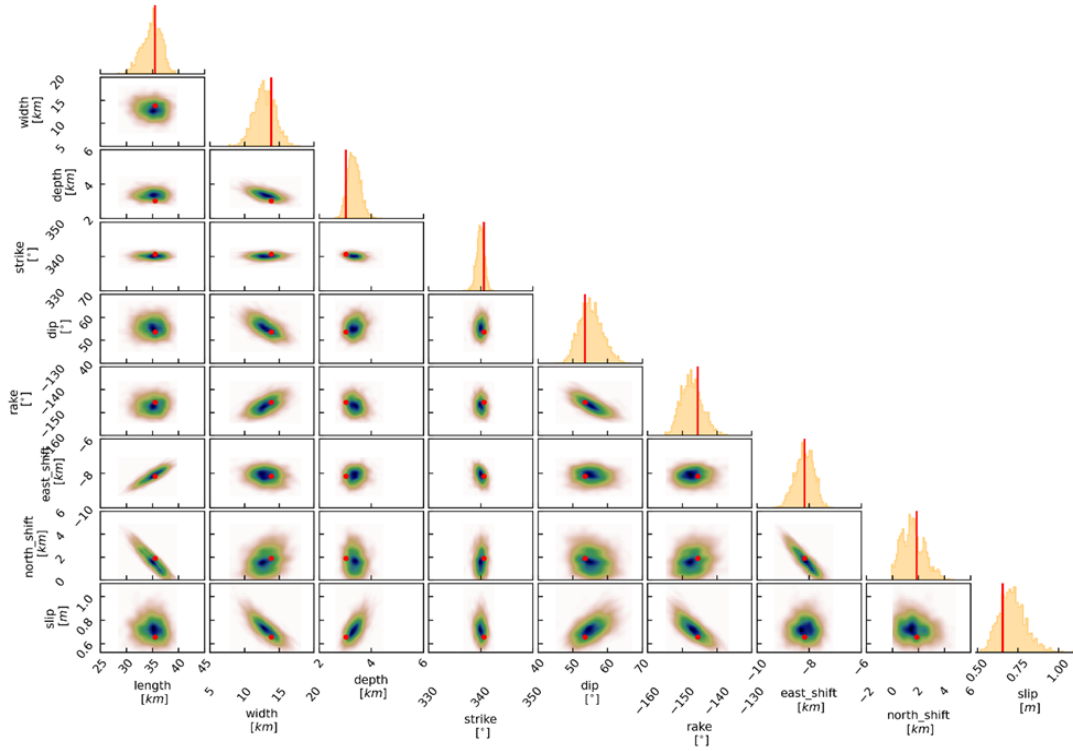|							
IPGP	100.443	51.241	13	358/237	46/62	-139/-52	6.84
GSRAS	100.42	51.32	20	29/228	46/46	-103/0	Mb 6.5
This study	$100.33^{+0.01}_{-0.01}$	$51.34^{+0.01}_{-0.02}$	$8.9^{+0.6}_{-0.2}$	$340.4^{+1.0}_{-1.6}$	$53.9^{+7.0}_{-4.0}$	$-146.4^{+4.6}_{-5.8}$	$6.75^{+0.13}_{-0.17}$

Fig. 4. Posterior probability distributions for the fault model parameters of the 2021 Hovsgol earthquake. Red lines and cycles represent the maximum-a-posteriori probability solution. Scatter plots are contoured according to frequency (cold colors for high frequency, warm colors for low frequency).

The optimal coseismic slip inversion results indicate that the 2021 Turt earthquake ruptured on a fault structure with a length of ~35 km (coseismic slip > 0.2m) along the west bank of Lake Hovsgol (Fig. 5), which successfully reproduces the InSAR observations (Fig. 3). The RMS of observations and model predictions are about 1 cm for InSAR observations. The coseismic slip is mainly concentrated at depths of 2-10 km with a peak slip of 1.2 m located at 7 km depth. The uncertainty of slip on each patch is marked by ellipses in Fig. 5. Assuming the average shear moduli is 34 GPa in the Hovsgol region (Laske et al., 2013), we calculated a geodetic moment (M_0) as ~2.46×10^{19} Nm. The estimated geodetic moment is corresponding to M_w 6.75, which is generally consistent with different catalogs (Table 1). Interestingly, the finite coseismic fault slip reveals that the slip is characterized by comparable dip-slip and right-lateral slip component (rake = -146°). In addition, no obvious shallow (0-2

288   km in depth) coseismic slip may indicate the shallow slip deficit (Xu et al., 2019).
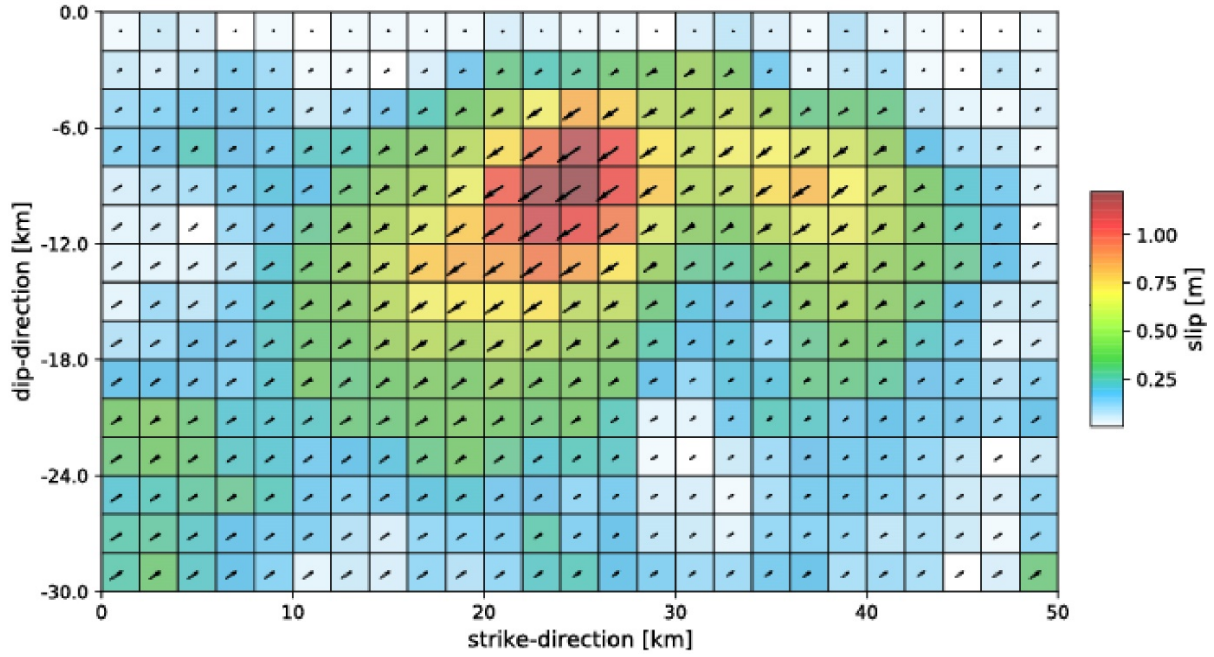

289

Fig. 5. Coseismic slip distribution solution for the 2021 Turt earthquake estimated using InSAR interferogram. The color patches and black arrows show the value and direction of the maximum-a-posterior solution. The two-sigma confidence interval is indicated by black ellipses around the arrow tips.

3.3. Stress inversion

The achieved stress inversion results are reported and summarized in Fig. 6 and Table 2, showing the stress fields in and around the Hovsgol basin is rather complicated. The sub-horizontal σ_1 axes in North Hovsgol Region (NHR) with NE-SW orientation and a low R (0.3) value indicating slightly difference in magnitude between σ_1 and σ_2 (Fig. 6b), coupled with horizontal σ_3 (Table 2), implies the NHR is under coexistence of both normal and strike slip stress regimes. The NHR is characterized by well-defined 95% confidence regions of sub-horizontal principal stress σ_3. In addition, we inverted all the compiled focal mechanisms for average stress filled in and around Hovsgol basin (Fig. 6a and c). It is similar to the stress filed of NHR but with much large average misfit angle 57°, indicating the background tectonics stress fields in and around Hovsgol basin are highly heterogenous (Michael, 1991).

Table 2. Stress tensor parameters as obtained from focal mechanisms inversion

Subregions	N[a]	σ_1 (°) az./pl.[b]	σ_2 (°) az./pl.	σ_3 (°) az./pl.	R	α(°)	Stress Regime	SHmax[c]
North Hovsgol	15	223/48	34/42	128/4	0.30	43	NS	38
Total region	29	250/45	32/38	138/20	0.34	57	NS	48

[a] Number of focal mechanisms; [b] Azimuth and plunge angles; [c] maximum horizontal compressive stress orientation.

According to the scheme of stress regime characterization and maximum horizontal compressive stress orientation (SHmax) proposed by (Zoback, 1992) based on the plunge and azimuth angles of stress axes, the results for the NHR and the entire study region show that it is under transtension stress field. The estimated SHmax in the 2021 Turt earthquake region is 38° (Table 2). This is consistent with our observed transtensional fault slip (Fig. 5) and comparable with the data (SHmax 23°/31°) from World Stress Map project (Heidbach et al., 2016).
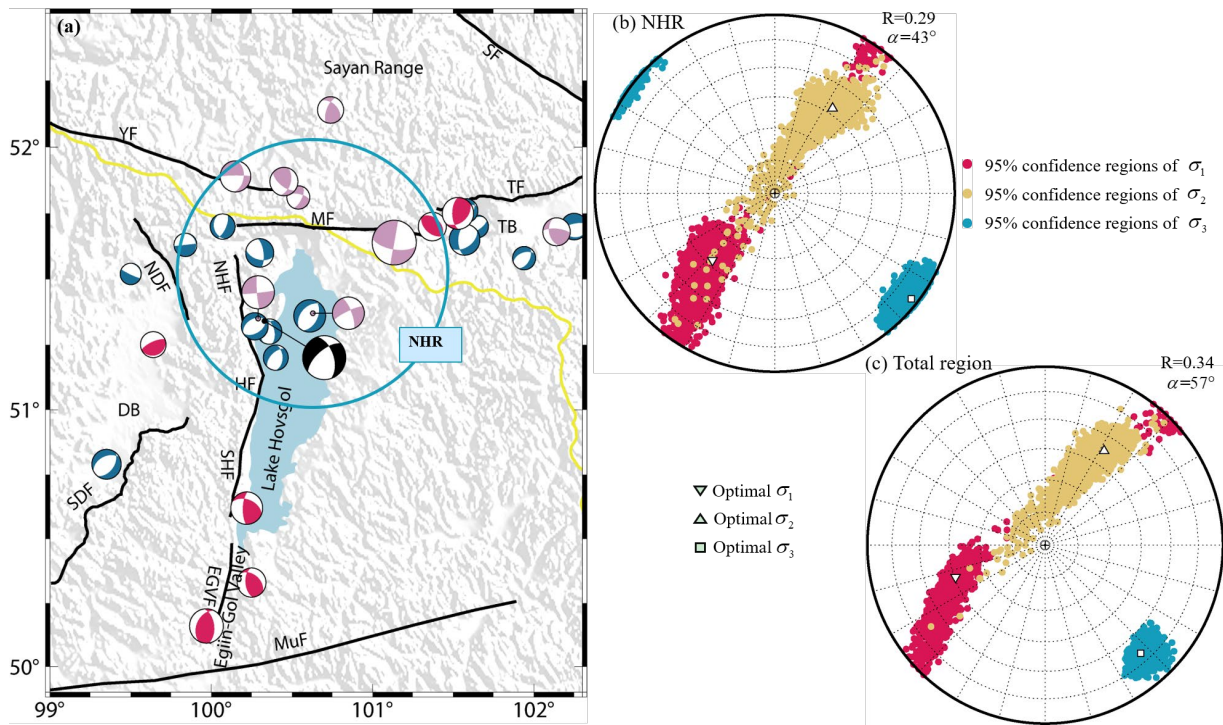

Fig. 6. The stress tensor inversion. (a) Focal mechanisms in the lower hemisphere projection used in the stress inversion for the entire region and for the northern part of the Hovsgol basin; (b) results of stress inversion for the northern part of the Hovsgol area; (c) results of stress inversion for the entire region.

4. Discussion

4.1. Faulting and stress heterogeneity in the Hovsgol basin region

The 2021 Mw 6.7 Turt earthquake is the largest instrumentally recorded event occurred within the Hovsgol basin. It is supposed to be caused by movement on the NW striking plane resulting from normal faulting with a right-lateral strike-slip component. The solution obtained in our study is in agreement with tensor moments issued by GCMT and IPGP, while other available solutions show mostly normal faulting (Fig. 1b and Table 1). The type of displacement in our focal mechanism corresponds to the kinematics of the NW fault determined from geological-structural data (Sankov et al., 2004). The field data described in (Sankov et al., 2004) also show, along with facets characterizing normal fault movements, regular right-lateral shear displacements of high-order stream valleys and asymmetric fanning cones. The stress regime deduced from the mainshock and previous focal mechanisms is transtension (Table 2); while earlier it was defined as pure extensive (Delouis et al., 2002). Since the stress inversion results are highly dependent on the input events, we argue that the completer and more up-to-date catalog in our study provide a more compelling evidence. Thus, we can state that the northern part of the Hovsgol basin is under extensional conditions with a right strike-slip component on NW oriented faults. This extension seems to be local because it is surrounded by transpression and strike-slip stress regimes (Delouis et al., 2002; Melnikova et al., 2004; Radziminovich et al., 2016; Sankov et al., 2004). Spatially, the present-day stress field in the region is changing from compression in the southern part of the Hovsgol basin to extension in its northern part, and then, to the north of the Hovsgol basin, the stress field is transpressive (Delouis et al., 2002; Melnikova et al., 2004; Radziminovich et al., 2016; Sankov et al., 2004). This complex spatial stress regime transition is probably responsible for the large average misfit angle in the stress inversion for the entire considered region (Fig.5, Table 2).

This indicates the complicated stress heterogeneity within the Hovsgol region, which can be deduced from the stress inversion results in and around the Hovsgol basin (Fig. 6). It is also visible from the basin morphology which shows a widespread deforming zone in the north but relatively narrow rift in the south (Fig. 7). Specifically, the topography is relatively lower in the southern counterpart. Gravity data also indicates remarking sedimentary thickness difference between north and south of the Hovsgol depression, with the maximum

550 m of sediments confined to the northern part of the depression, while the thickness of sediments rarely exceeds 350 m in the southern part of the Lake Hovsgol (Gladkochub and Donskaya, 2009; Zorin et al., 1989).

Reasons for heterogeneity of the stress field in the region are still under discussion. The local extension, for example, was modeled as opening of the northern basin which is in a T-shape conjunction of the Mondy fault and Hovsgol fault, and the diagonal NW fault forms the block structure of this area (Sankov et al., 2004). After the Turt earthquake, most of aftershocks (~60,000 in the first three months) from local seismic stations, are located in the conjugate angle region between near E-W MF and NW-S NHF, confirming activity of this block of the crust. In addition, stress heterogeneity including stress orientations and concentrations is attributed to active fault structures (Petit et al., 1996; Wilson et al., 2009; Yale, 2003) and contrasting rheology (Wileveau et al., 2007). Petit et al. (Petit et al., 1996) suggest that inherited structures have a crucial influence on the local stress field changes within the Baikal rift zone, so that changes in stresses are spatially confined to changes in the Siberian craton boundary. The sudden fault strike changes from near E-W direction (YF, MF and TF) to near N-S direction (HF, NDF and SDF), and then to NEE-SWW (MuF) orientation is observed in the Hovsgol region (Fig. 1b, Fig. 7), which may geometrically control the stress heterogeneity from north to south here.

Fault strike change is observed also along the western side of the Hovsgol basin, from SHF (10°) to NHF (341°). According to some study (Nicol et al., 2005; Wilson et al., 2009), the fault linkage point may control the displacements on the faults, so this change along the Hovsgol fault may inhibit the rupture propagation to SHF, confirming by the coseismic displacement mainly confined surrounding NHF during the Turt earthquake (Fig. 3). In this regard, it should be noted that seismicity of the instrumental period is concentrated in the northern part and southern tip of the Lake Hovsgol, while the south-central part of the lake (50.5° N - 51° N) seems to be a seismic gap where few earthquakes have been recorded (Dugarmaa et al., 2002; Radziminovich et al., 2016) (Fig.1).

4.2. Half-graben-dominated depression

Hovsgol basin is generally considered as the result of subsidence on the down-dropped block of half-graben with the master steep western HF hosting the 2021 mainshock. Some

388　literature only propose the active western major HF which is clear on the topography and

389　geomorphology (Ivanov et al., 2015; Pollitz et al., 2003; Ritz et al., 2018). Some others, however,

390　show the eastern minor Hovsgol fault (Petit et al., 1996; Tapponnier and Molnar, 1979; Wang et

391　al., 2013). This makes it confused whether Hovsgol basin is dominated by half- or full-graben.

392　Our geodetic observations show a dominated subsidence observed near the major HF on the

393　western side indicating that the current subsidence is dominated by half-graben depression

394　(Fig. 3). Epicenter distribution of the previous seismicity (Dugarmaa et al., 2002), as well as

395　aftershocks following the 2021 Turt earthquake show that much intense seismic activities is

396　observed on the west side of Lake Hovsgol compared with the east side.

397　　　Lithology of the basin sides differs; Pliocene basalts are located on the eastern side of HF,

398　while it is relatively complex with sedimentary volcanic units (Riphean), Oselkovaya

399　sedimentary series (Early Vendian) and Dzhidinsky sedimentary sequence (Middle Cambrian)

400　on the western side (Fig. S3, http://bic.iwlearn.org/en/atlas/atlas-of-the-baikal-basin-

401　eng/view). Bathymetry data of Lake Hovsgol indicates that the slope of the bottom of the lake

402　is steep on the west and gentle on the east (Fig. 7), which is consistent with the observed fault

403　scarps and steep slope on the west. This is also consistent with the west dome-blocky uplift

404　and east arch-like structure features within Hovsgol basin (Gladkochub and Donskaya, 2009).

405　Thus, the dominated west InSAR subsidence zone and remarkable difference of lithology,

406　seismic activity, lake bathymetry, geomorphology fault scarps indicate that the current

407　Hovsgol basin is still dominated by half-graben. Interestingly, the coseismic InSAR

408　observations also show surface displacement on eastern Lake Hovsgol bank (Fig. 3), implying

409　the potential local structures. Aftershocks from local seismic stations show microearthquake

410　(ML ~2) cluster which agrees well with the displacement zone on eastern bank of Lake

411　Hovsgol. These indicate that the minor structure may be activated by the 2021 Turt
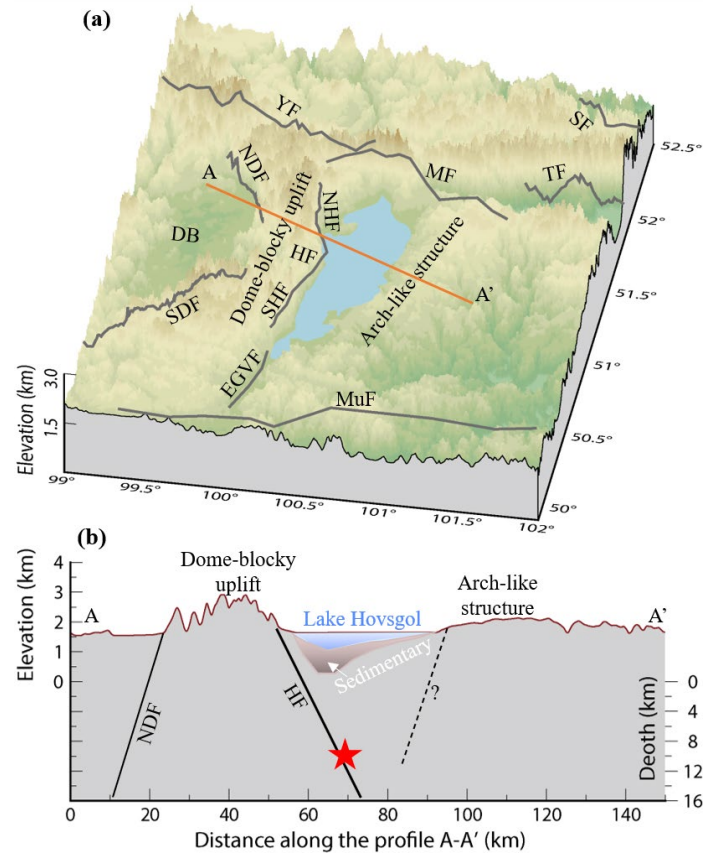
412　earthquake (Fig. 7b).

413

Fig. 7. Topography of the region. (a) The 3D view of topography in Fig. 1b. Gray lines represent active faults. The fault abbreviations are identical to those in Fig. 1. Orange line is the profile A-A' shown in (b). (b) The 2D conceptional model on the profile A-A'. Solid and dashed black lines represent the seismogenic fault and a possible oppositely dipping fault beneath the eastern bank of Lake Hovsgol. Red star indicates the hypocenter of the 2021 Turt earthquake.

4.3. Regional Seismic Hazard

Considering the complicated heterogeneity stress background in the Hovsgol region, it is crucial to evaluate the influence of 2021 Turt earthquake on its surrounding active faults. Seismic stress triggering theory indicates that accumulated tectonic stress is suddenly released during earthquakes, the redistributed stress may influence the adjacent faults with stress triggers promoting the subsequent seismicity or stress shadows delaying the subsequent earthquake ruptures (Harris, 1998; King et al., 1994; Stein et al., 1994). Utilizing the coseismic slip model caused by the 2021 Turt earthquake as the driving source, and assuming the effective coefficient of $\mu=0.4$, we estimated the static Coulomb Failure Stress changes (ΔCFS)

430 triggered by the mainshock on the surrounding active faults (Lin and Stein, 2004; Toda et al.,
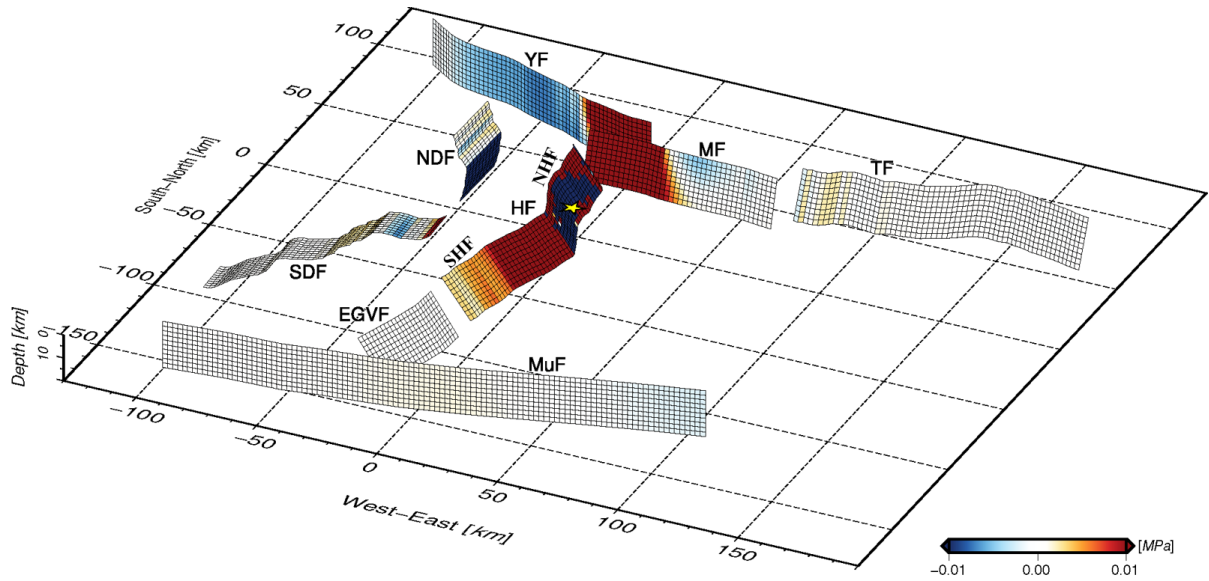
431 2005).

432

Fig. 8. Distribution of the static ΔCFS in the adjacent active faults induced by the 2021 Turt

434 earthquake. The fault abbreviations are identical to those in Fig. 1b. Yellow star represents the

435 USGS hypocenter. The geometries of the receiver faults are determined based on the

436 information of regional moment tensor and GEM Global Active Faults (Table S4).

437

438 The maximum positive and negative static ΔCFS both about 2.5 MPa are found on the

439 NHF (Fig. 8 and Fig. S4). It is worth noting that color scale is saturated at [-0.01 0.01] MPa

440 for the visualization (Fig. 8). Strong stress triggers around coseismic rupture zone on NHF

441 may explain the aftershocks after the mainshock and indicates potential postseismic transients

442 (e.g., afterslip, poroelastic rebound, and viscoelastic relaxation). Stress triggers (0.16 MPa,

443 Fig. 8 and Table S4) are found on the west Mondy Fault, a sinistral strike slip fault dipping

444 south which hosted the 1950 Mondy Mw 6.9 (Delouis et al., 2002). In addition, 0.03 MPa stress

445 triggers are observed on the east tip of YF (Fig. 8 and Table S4); whereas the NDF, west YF

446 and east MF are mainly located in a stress shadow zone. It is obviously that the geometries of

447 receiver faults play an important role in the ΔCFS calculations. For instance, the striking

448 orientation changes are significantly influence the polarity (stress triggers or stress shadows)

449 of ΔCFS , which can be observed clearly on fault NDF and SDF (Fig. 8). This kind of

450 structure-orientation-related ΔCFS polarity is also reported, for example, in the case of 2020

451 Mw 6.5 Monte Cristo Range Earthquake (Zheng et al., 2020). This seems further confirming

452   that the strikes change is one of the potential reasons for the stress heterogeneity in Hovsgol

453   region. The calculated positive ΔCFS on the northward faults (east YF, west MF and central

454   MuF) exceeds the earthquake triggering threshold 0.01 MPa (Hardebeck et al., 1998). This

455   indicates that the seismic hazard for these faults may be potentially increased, especially for

456   the West Mondy Fault. Besides, rather strong positive ΔCFS (~0.5 MPa, Fig. 8 and Table S4)

457   are observed on the SHF induced by the 2021 Turt earthquake. Considering that the SHF is a

458   seismic gap during the instrumental era, we suggest that potential seismic hazard on SHF
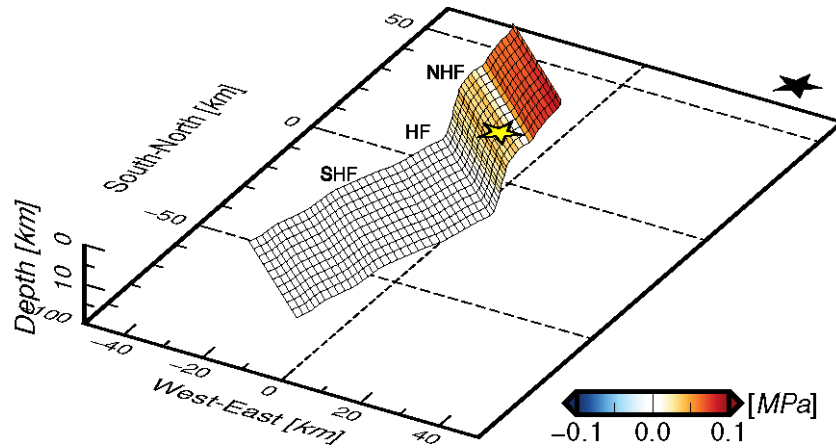
459   should be also taken into consideration.

460

461   **Fig. 9.** Distribution of the static ΔCFS on the Hovsgol Fault induced by the 1950 Mondy Mw

462   6.9 earthquake. The effective friction coefficient is 0.4. The fault abbreviations are identical to

463   those in Fig. 1b. Yellow and black stars represent the hypocenter of 2021 Turt earthquake and

464   1950 Mondy earthquake, respectively.

465   In addition, considering that the 1950 Mondy Mw 6.9 and the 2021 Turt Mw 6.7

466   earthquakes are only ~70 km apart, we modeled the possible impact of the Mondy fault.

467   Based on the focal mechanism of 1950 Mondy earthquake (Delouis et al., 2002), we synthesized

468   the uniform pure sinistral coseismic slip (0.83 m) on a 50 km×20 km fault plane with strike

469   100° and dip 75°. With the same method above, the static Coulomb Failure Stress changes

470   (ΔCFS) triggered by the 1950 Mondy earthquake were estimated on the Hovsgol Fault (Figs.

471   9 and S5). Almost all positive static ΔCFS with an average value of 0.05 MPa are located on

472   the NHF, indicating that the 1950 Mondy event may significantly promote the 2021 Turt

473   earthquake. Given the average stress drop of about 0.72 MPa in the 2021 rupture zone and

474   assuming recurrence earthquake releasing the same tectonic stress, we suggest that the 1950

475   event advanced the 2021 earthquake by about 7% recurrence interval. However, it seems to

476   have little positive effect on SHF and shows stress shadow with a peak value of -0.008 MPa

477   inhibiting earthquake nucleation on the north tip of the SHF (Figs. 9 and S5). This may

478   explain, to some degree, the seismic gap on SHF and seems to evidence again that structures

479   geometry plays a significant role in local stress field.

480

5. Conclusions

482   In this study, we investigated the seismogenic fault geometry, coseismic fault slip with

483   surface displacement fields for the Mw6.7 2021 Turt earthquake by using InSAR and

484   teleseismic data. We found that the observations can be best explained by the fault slip on a

485   seismogenic fault with a strike of 341° and a dip angle of 54°. Coseismic slip is characterized

486   by normal faulting with a dextral strike-slip component with a peak value of 1.2 m at 7 km

487   depth. According to InSAR data, up to ~20 cm surface subsidence occurred at the hanging

488   wall of the fault. The stress inversion results show that this earthquake occurred within a

489   transtensive stress regime. It is a local area with such a regime being surrounded by

490   transpressive and strike-slip stress fields. This stress heterogeneity is probably controlled by

491   the distinct structure geometries in and around Hovsgol basin.

492   The dominated west bank InSAR subsidence and remarkable difference of lithology,

493   seismic activity, lake bottom slope, geomorphology fault scarps, indicate that the current

494   Hovsgol basin is still dominated by half-graben. The calculated ΔCFS induced by the 2021

495   Turt earthquake suggests the potential seismic hazard associated with the West Mondy Fault

496   that deserves further attention. In addition, the ΔCFS caused by the 1950 Mondy earthquake

497   may advance the 2021 Turt earthquake by ~7% recurrence interval. The findings reported here

498   have important implications for regional heterogenous stress field of the crust, graben

499   deformation mechanisms and seismic potential.

500

501

Author Contributions

X.L. and W.X. designed the study, organized experimental work. X.L. wrote the original manuscript. X.L. and N.F. conducted the experimental work. X.L., W.X. and N.A.R. led the writing of the manuscript with contributions from all coauthors. All authors commented on, reviewed, and edited the presented version of manuscript.

Competing Interests

The authors declare that they have no competing interests.

Data Availability Statement

Raw Sentinel-1A data are available from https://scihub.copernicus.eu/dhus/#/home. Seismic data are accessed from IRIS (https://ds.iris.edu). The processed data used in the study are available (https://doi.org/10.5281/zenodo.5078988). The GAMMA commercial software is obtained from https://www.gamma-rs.ch/software. The BEAT software is obtained from https://github.com/hvasbath/beat. The iterative joint stress inversion software is obtained from https://www.ig.cas.cz/en/stress-inverse/. The Coulomb3 software is available from https://www.usgs.gov/software/coulomb-3. The Generic Mapping Tools (Wessel et al., 2013) created figures are obtained from https://www.genericmapping-tools.org/.

References

Bayasgalan, A., Jackson, J., McKenzie, D., 2005. Lithosphere rheology and active tectonics in Mongolia: relations between earthquake source parameters, gravity and GPS measurements. Geophysical Journal International 163, 1151-1179.

Calais, E., Vergnolle, M., San'kov, V., Lukhnev, A., Miroshnitchenko, A., Amarjargal, S., Déverchère, J., 2003. GPS measurements of crustal deformation in the Baikal-Mongolia area (1994-2002): Implications for current kinematics of Asia. Journal of Geophysical Research: Solid Earth 108.

Chen, C.W., Zebker, H.A., 2001. Two-dimensional phase unwrapping with use of statistical models for cost functions in nonlinear optimization. Journal of the Optical Society of America a-Optics Image Science and Vision 18, 338-351.

Del Moral, P., Doucet, A., Jasra, A., 2006. Sequential monte carlo samplers. Journal of the Royal Statistical Society: Series B (Statistical Methodology) 68, 411-436.

Delouis, B., Déverchère, J., Melnikova, V., Radziminovitch, N., Loncke, L., Larroque, C., Ritz, J., San'kov, V., 2002. A reappraisal of the 1950 (Mw 6.9) Mondy earthquake, Siberia, and its relationship to the strain pattern at the south-western end of the Baikal rift zone. Terra Nova 14, 491-500.

Dobrynina, A.A., Sankov, V.A., Tcydypova, L.R., German, V.I., Chechelnitsky, V.V., Ulzibat, M., 2018. Hovsgol earthquake 5 December 2014, MW = 4.9: seismic and acoustic effects. Journal of Seismology 22, 377-389.

Dugarmaa, T., Schlupp, A., Adija, M., Ankhtsetseg, D., Bayar, G., Munkhuu, D., Selenge, L., Tsembel, B., Ulziibat, M., Odonbaatar, C., 2002. Seismic Map of Mongolia and Site Effect Microzoning at the Capital, Ulaanbaatar, AGU Fall Meeting Abstracts, pp. S71B-1100.

Farr, T.G., Rosen, P.A., Caro, E., Crippen, R., Duren, R., Hensley, S., Kobrick, M., Paller, M., Rodriguez, E., Roth, L., Seal, D., Shaffer, S., Shimada, J., Umland, J., Werner, M., Oskin, M., Burbank, D., Alsdorf, D., 2007. The shuttle

548   radar topography mission. Reviews of Geophysics 45.

549   Gephart, J.W., Forsyth, D.W., 1984. An improved method for determining the regional stress tensor using

550   earthquake focal mechanism data: application to the San Fernando earthquake sequence. Journal of

551   Geophysical Research: Solid Earth 89, 9305-9320.

552   Gladkochub, D., Donskaya, T., 2009. Overview of geology and tectonic evolution of the Baikal-Tuva area,

553   Biosilica in Evolution, Morphogenesis, and Nanobiotechnology. Springer, pp. 3-26.

554   Hardebeck, J.L., Nazareth, J.J., Hauksson, E., 1998. The static stress change triggering model: Constraints

555   from two southern California aftershock sequences. Journal of Geophysical Research: Solid Earth 103,

556   24427-24437.

557   Harris, R.A., 1998. Introduction to Special Section: Stress Triggers, Stress Shadows, and Implications for

558   Seismic Hazard. Journal of Geophysical Research: Solid Earth 103, 24347-24358.

559   Heidbach, O., Rajabi, M., Reiter, K., Ziegler, M., 2016. WSM-World Stress Map Database Release. GFZ Data

560   Services. http//: doi. org/10.5880/WSM.

561   Ivanov, A.V., Demonterova, E.I., He, H., Perepelov, A.B., Travin, A.V., Lebedev, V.A., 2015. Volcanism in the

562   Baikal rift: 40years of active-versus-passive model discussion. Earth-Science Reviews 148, 18-43.

563   Jolivet, M., Arzhannikov, S., Chauvet, A., Arzhannikova, A., Vassallo, R., Kulagina, N., Akulova, V., 2013.

564   Accommodating large-scale intracontinental extension and compression in a single stress-field: A key

565   example from the Baikal Rift System. Gondwana Research 24, 918-935.

566   Jónsson, S., Zebker, H., Segall, P., Amelung, F., 2002. Fault slip distribution of the 1999 M w 7.1 Hector Mine,

567   California, earthquake, estimated from satellite radar and GPS measurements. Bulletin of the Seismological

568   Society of America 92, 1377-1389.

569   King, G.C., Stein, R.S., Lin, J., 1994. Static stress changes and the triggering of earthquakes. Bulletin of the

570   Seismological Society of America 84, 935-953.

571   Laske, G., Masters, G., Ma, Z., Pasyanos, M., 2013. Update on CRUST1. 0—A 1-degree global model of Earth's

572   crust, Geophys. Res. Abstr, p. 2658.

573   Li, Z., Ding, X., Huang, C., Zhu, J., Chen, Y., 2008. Improved filtering parameter determination for the

574   Goldstein radar interferogram filter. ISPRS Journal of Photogrammetry and Remote Sensing 63, 621-634.

575   Lin, J., Stein, R.S., 2004. Stress triggering in thrust and subduction earthquakes and stress interaction

576   between the southern San Andreas and nearby thrust and strike-slip faults. Journal of Geophysical

577   Research: Solid Earth 109.

578   Liu, X., Xu, W., 2019. Logarithmic model joint inversion method for coseismic and postseismic slip:

579   Application to the 2017 Mw 7.3 Sarpol Zahāb earthquake, Iran. Journal of Geophysical Research: Solid

580   Earth 124, 12034-12052.

581   Lund, B., Slunga, R., 1999. Stress tensor inversion using detailed microearthquake information and stability

582   constraints: Application to Ölfus in southwest Iceland. Journal of Geophysical Research: Solid Earth 104,

583   14947-14964.

584   Martínez-Garzón, P., Ben-Zion, Y., Abolfathian, N., Kwiatek, G., Bohnhoff, M., 2016. A refined methodology for

585   stress inversions of earthquake focal mechanisms. Journal of Geophysical Research: Solid Earth 121, 8666-

586   8687.

587   Melnikova, V.I., A., G.N., A.I., S., 2020. Catalogue of earthquake focal mechanisms for the Baikal region for

588   2014 In: Earthquakes of the Northern Eurasia, Obninsk, GS RAS

589

590   Melnikova, V.I., Radziminovich, N.A., Adyaa, M., 2004. Mechanisms of earthquake foci and seismotectonic

591   deformations of the Mongolia region. Complex geophysical and seismological investigations in Mongolia.

592   Research Centre of Astronomy and Geophysics of the Mongolian Academy of Sciences, Ulaanbaatar, 165-170.

593   Meltzer, A., Stachnik, J.C., Sodnomsambuu, D., Munkhuu, U., Tsagaan, B., Dashdondog, M., Russo, R., 2019. The

594 Central Mongolia Seismic Experiment: Multiple Applications of Temporary Broadband Seismic Arrays.
595 Seismological Research Letters 90, 1364-1376.

596 Michael, A.J., 1984. Determination of stress from slip data: faults and folds. Journal of Geophysical Research:
597 Solid Earth 89, 11517-11526.

598 Michael, A.J., 1987. Use of focal mechanisms to determine stress: a control study. Journal of Geophysical
599 Research: Solid Earth 92, 357-368.

600 Michael, A.J., 1991. Spatial variations in stress within the 1987 Whittier Narrows, California, aftershock
601 sequence: New techniques and results. Journal of Geophysical Research: Solid Earth 96, 6303-6319.

602 Nicol, A., Walsh, J., Berryman, K., Nodder, S., 2005. Growth of a normal fault by the accumulation of slip over
603 millions of years. Journal of Structural Geology 27, 327-342.

604 Petit, C., Déverchère, J., 2006. Structure and evolution of the Baikal rift: A synthesis. Geochemistry,
605 Geophysics, Geosystems 7.

606 Petit, C., Déverchère, J., Calais, E., San'kov, V., Fairhead, D., 2002. Deep structure and mechanical behavior of
607 the lithosphere in the Hangai–Hövsgöl region, Mongolia: new constraints from gravity modeling. Earth and
608 Planetary Science Letters 197, 133-149.

609 Petit, C., Déverchère, J., Houdry, F., Sankov, V.A., Melnikova, V.I., Delvaux, D., 1996. Present-day stress field
610 changes along the Baikal rift and tectonic implications. Tectonics 15, 1171-1191.

611 Pollitz, F., Vergnolle, M., Calais, E., 2003. Fault interaction and stress triggering of twentieth century
612 earthquakes in Mongolia. Journal of Geophysical Research: Solid Earth 108.

613 Radziminovich, N.A., Bayar, G., Miroshnichenko, A.I., Demberel, S., Ulziibat, M., Ganzorig, D., Lukhnev, A.V.,
614 2016. Focal mechanisms of earthquakes and stress field of the crust in Mongolia and its surroundings.
615 Geodynamics & Tectonophysics 7, 23-38.

616 Ritz, J., Larroque, C., Stephan, J., San'kov, V., Arjannikova, A., Calais, E., Deverchere, J., Loncke, L., 2000. When
617 compression meets extension: interaction or competition? The example of the Tunka basin (Western Baikal,
618 Siberia). Proceedings of the Geosciences, 122.

619 Ritz, J.F., Arzhannikova, A., Vassallo, R., Arzhannikov, S., Larroque, C., Michelot, J.L., Massault, M., 2018.
620 Characterizing the Present-Day Activity of the Tunka and Sayan Faults Within Their Relay Zone (Western
621 Baikal Rift System, Russia). Tectonics 37, 1376-1392.

622 Sankov, V.A., Microshnichenko, A.I., Parfeevets, A.V., Arzhannikova, A.V., Lukhnev, A.V., 2004. Late Cenozoic
623 state of stress in the Earth's crust of the Khubsugul region (Northern Mongolia): Field and experimental
624 evidence. Geotectonics 38, 142-152.

625 Sankov, V.A., Parfeevets, A.V., Lukhnev, A.V., Miroshnichenko, A.I., Ashurkov, S.V., 2011. Late Cenozoic
626 geodynamics and mechanical coupling of crustal and upper mantle deformations in the Mongolia-Siberia
627 mobile area. Geotectonics 45, 378-393.

628 Schlupp, A., Cisternas, A., 2007. Source history of the 1905 great Mongolian earthquakes (Tsetserleg,
629 Bolnay). Geophysical Journal International 169, 1115-1131.

630 Stein, R.S., King, G.C., Lin, J., 1994. Stress triggering of the 1994 M= 6.7 Northridge, California, earthquake by
631 its predecessors. Science 265, 1432-1435.

632 Tapponnier, P., Molnar, P., 1979. Active faulting and cenozoic tectonics of the Tien Shan, Mongolia, and
633 Baykal Regions. Journal of Geophysical Research: Solid Earth 84, 3425-3459.

634 Toda, S., Stein, R.S., Richards-Dinger, K., Bozkurt, S.B., 2005. Forecasting the evolution of seismicity in
635 southern California: Animations built on earthquake stress transfer. Journal of Geophysical Research: Solid
636 Earth 110.

637 Vasiliev, E.P., Belichenko, V.G., Reznitskii, L.Z., 1997. Relationship between Ancient and Cenozoic structures
638 at the Southwestern flank of the Baikal rift zone. Doklady Academii Nauk 353, 789-792.

639 Vasyura-Bathke, H., Dettmer, J., Steinberg, A., Heimann, S., Isken, M.P., Zielke, O., Mai, P.M., Sudhaus, H.,

640 Jónsson, S., 2020. The Bayesian earthquake analysis tool. Seismological Research Letters 91, 1003-1018.

641 Vavryčuk, V., 2014. Iterative joint inversion for stress and fault orientations from focal mechanisms.
642 Geophysical Journal International 199, 69-77.

643 Vavryčuk, V., Bouchaala, F., Fischer, T., 2013. High-resolution fault image from accurate locations and focal
644 mechanisms of the 2008 swarm earthquakes in West Bohemia, Czech Republic. Tectonophysics 590, 189-
645 195.

646 Vergnolle, M., Pollitz, F., Calais, E., 2003. Constraints on the viscosity of the continental crust and mantle from
647 GPS measurements and postseismic deformation models in western Mongolia. Journal of Geophysical
648 Research: Solid Earth 108.

649 Wald, D.J., Heaton, T.H., Hudnut, K.W., 1996. The slip history of the 1994 Northridge, California, earthquake
650 determined from strong-motion, teleseismic, GPS, and leveling data. Bulletin of the Seismological Society of
651 America 86, S49-S70.

652 Wang, M., Shen, Z.K., 2020. Present-Day Crustal Deformation of Continental China Derived From GPS and
653 Its Tectonic Implications. Journal of Geophysical Research: Solid Earth 125.

654 Wang, S., Pei, S., Xu, G., Gao, A., 2013. Pn velocity structure at the uppermost mantle of Mongolia and
655 neighboring regions. Chinese Journal of Geophysics 56, 4106-4112.

656 Warren-Smith, E., Fry, B., Wallace, L., Chon, E., Henrys, S., Sheehan, A., Mochizuki, K., Schwartz, S., Webb, S.,
657 Lebedev, S., 2019. Episodic stress and fluid pressure cycling in subducting oceanic crust during slow slip.
658 Nature Geoscience 12, 475-481.

659 Wegmuller, U., Werner, C., Stroozzi, T., Wiesmann, A., Frey, O., Santoro, M., 2015. Sentinel-1 support in the
660 GAMMA Software. ESASP 731, 33.

661 Wessel, P., Smith, W.H., Scharroo, R., Luis, J., Wobbe, F., 2013. Generic mapping tools: improved version
662 released. Eos, Transactions American Geophysical Union 94, 409-410.

663 Wileveau, Y., Cornet, F., Desroches, J., Blumling, P., 2007. Complete in situ stress determination in an argillite
664 sedimentary formation. Physics and Chemistry of the Earth, Parts A/B/C 32, 866-878.

665 Wilson, P., Hodgetts, D., Rarity, F., Gawthorpe, R.L., Sharp, I.R., 2009. Structural geology and 4D evolution of a
666 half-graben: New digital outcrop modelling techniques applied to the Nukhul half-graben, Suez rift, Egypt.
667 Journal of Structural Geology 31, 328-345.

668 Xu, G., Xu, C., Wen, Y., Yin, Z., 2019. Coseismic and Postseismic Deformation of the 2016 MW 6.2 Lampa
669 Earthquake, Southern Peru, Constrained by Interferometric Synthetic Aperture Radar. Journal of
670 Geophysical Research: Solid Earth 124, 4250-4272.

671 Xu, W.B., 2017. Finite-fault slip model of the 2016 M-w 7.5 Chiloe earthquake, southern Chile, estimated
672 from Sentinel-1 data. Geophysical Research Letters 44, 4774-4780.

673 Xu, W.B., Rivalta, E., Li, X., 2017. Magmatic architecture within a rift segment: Articulate axial magma storage
674 at Erta Ale volcano, Ethiopia. Earth and Planetary Science Letters 476, 79-86.

675 Yale, D.P., 2003. Fault and stress magnitude controls on variations in the orientation of in situ stress.
676 Geological Society, London, Special Publications 209, 55-64.

677 Zheng, A., Chen, X., Xu, W., 2020. Present-day deformation mechanism of the northeastern Mina deflection
678 revealed by the 2020 Mw 6.5 Monte Cristo Range earthquake. Geophysical Research Letters.

679 Zoback, M.L., 1992. First- and second-order patterns of stress in the lithosphere: The World Stress Map
680 Project. Journal of Geophysical Research 97.

681 Zorin, Y.A., Tumtanov, E.K., Arvisbaatar, N., 1989. Structure of Cenozoic basins of the Prekhubsugul region
682 from gravity data. Russian Geology and Geophysics 10, 130-136.

683